# Detector Summary; $\tau$-charm Factory Workshop

Jasper Kirkby

CERN, Geneva, Switzerland

| | |
|---|---|
| J.E.Brau | University of Oregon, Eugene, OR 97403 |
| V.Lüth | Stanford Linear Accelerator Center, Stanford, CA 94305 |
| B.N.Ratcliff | Stanford Linear Accelerator Center, Stanford, CA 94305 |
| K.Sliwa | Tufts University, Medford, MA 02155 |
| R.Stroynowski | California Institute of Technology, Pasadena, CA 91125 |
| J.Thaler | University of Illinois, Urbana, IL 61801 |
| J.Va'vra | Stanford Linear Accelerator Center, Stanford, CA 94305 |
| A.Weinstein | California Institute of Technology, Pasadena, CA 91125 |

31 August 1989

During the Workshop the physics goals[1] of the $\tau$-charm Factory ($\tau$cF) were studied and their specific detector requirements evaluated. Based on these requirements and the constraints of the machine, the Detector Working Groups explored various approaches and arrived at a basic detector configuration, using existing technologies, that successfully meets the physics requirements. This configuration, which we summarize in this paper, involves a conceptual design with an initial specification of detector components, their locations and dimensions. No attempt was made at the Workshop to go into detailed aspects of the design or to optimize the materials, dimensions, granularities, etc; this next stage of the detector design is taking place over the coming months.

## 1 Introduction

The $\tau$-charm Factory will explore the second generation quark family and the third generation lepton family with unprecedented sensitivity. The success of this endeavour will depend on the combination of **two** features of the experimental apparatus:

| $\tau$cF **physics sensitivity** $\propto$ **machine luminosity x detector performance** |
|---|

The high luminosity of the $\tau$cF, combined with its unique operating points[1][2], will generate a large increase in the available statistics of $\tau$ and charm data samples, under conditions of low backgrounds and low systematic biases. As examples, the present total luminosity is 2 pb$^{-1}$ for $\tau$ studies below charm threshold, and 10 pb$^{-1}$ for charm studies at $\psi''(3.77)$. These figures may be compared with the design luminosity of $10^4$ pb$^{-1}$ per year at the $\tau$cF[3].

Furthermore, a substantial improvement can be made in detector performance compared with previous experiments. In particular, we note that no previous detector in the $\tau$-charm region has combined the advantages of the classical solenoidal magnetic detector – good momentum resolution and identification of charged particles – with the advantages of the crystal calorimeter detector – excellent energy resolution for $\gamma$, $e$, and $\pi^0$, and good low energy $\gamma$ detection efficiency. This style of detector – which has been pioneered by the work of L3 and CLEO II – would have a profound effect on the scope of physics accessible at the $\tau$cF, due to a sharp increase in the reconstruction efficiency and resolution of final states that include neutrals and due to improved $e$ identification.

The $\tau$-charm Factory is envisaged as a single fully-integrated experimental device comprising of a high performance machine **and** a high performance detector.

In the next section we will present the detector design criteria that emerged from the Workshop. This is followed by the technical considerations leading to the initial parameters of a detector that meets the physics requirements. We then describe both the basic $\tau$cF detector configuration and a modified version with improved particle identification. Finally, we summarize the performance of the $\tau$cF detector in comparison with Mark III, which exemplifies the present generation of detector at these energies.

# 2 Design criteria

The primary design requirements that emerged from the physics studies and discussions at the Workshop are as follows:

1. **Precise momentum measurement accuracy**, with particular emphasis on minimizing the effects of multiple Coulomb scattering:

$$[\sigma_p/p]^2 \;=\; [0.4\%p(\mathrm{GeV/c})]^2 + [0.3\%/\beta]^2$$

2. **Crystal electromagnetic calorimeter**, with high resolution of $\gamma$ energies:

$$[\sigma_E/E]^2 \;=\; [2\%/\sqrt{E\,(GeV)}]^2 + [1\%]^2$$

   and a low threshold energy for $\gamma$ detection:

$$E_\gamma^{min} \;\approx\; 10\mathrm{MeV}$$

3. **Excellent $\pi^\pm$, $K^\pm$ and $p$ separation**, with $\leq 10^{-2}$ misidentification probability below 1 GeV/c.

4. **Excellent $e$ and $\mu$ identification**, with $\leq 10^{-3}$ probability of misidentifying hadrons as electrons, and a few x $10^{-2}$ probability for $\pi/K$ to be identified as $\mu$.

5. **Hermeticity of the detector,** allowing for $\nu$ detection by missing energy. This can be achieved with an outer hadron calorimeter (tagger) and by eliminating blind regions in both the electromagnetic and hadronic calorimeters. The primary function of the hadron calorimeter is to tag the presence of neutral hadrons ($K_L^0/n$) which, if left undetected, would generate a background to the $\nu$ signal. After excluding such events, a precise determination of the missing energy can be made from the electromagnetic calorimetry and momentum measurements combined with particle identification. The detection inefficiencies are required to be below 1% in the electromagnetic calorimeter and below 5% in the hadronic calorimeter.

6. **Maximum-possible solid angle subtended in the barrel region.** This results in a large acceptance for the region of uncompromised performance: full tracking, precise $\sigma_p/p$, no end plate material, no detector boundaries, etc. The design goal is: $\Omega$ (barrel) $\approx$ 90% x $4\pi$ str.

7. **Conservative (wide) interaction-region vacuum chamber,** with a radius (50 mm) that is identical to the aperture elsewhere in the storage rings. This avoids the impedance and heating problems that can result from a narrow vacuum chamber at the interaction region of a high-current storage ring. A further advantage is that the angular resolution of charged tracks *improves* with a large-diameter vacuum chamber, after connecting the vertex with the impact point at the vacuum chamber wall.

8. **Advanced trigger/data acquisition system and off-line analysis farm.** Although the event rate off-resonance is low ($\leq$ 10 Hz), at $J/\psi$ it is several kHz, which implies the need for sophisticated triggering and a high-speed data acquisition system. The $\tau$cF will generate a large amount of data which will require a dedicated off-line analysis farm similar to the ACP at FNAL. (These aspects of the detector are presented elsewhere in these Proceedings[4,5], and are not discussed further here.)

A summary of the individual $\tau$cF experiments that led to the detector design criteria is given in Table 1. We add the following brief comments:

1. *Charged particles.* The main experiment which drives the precise $\sigma_p/p$ requirement is the $\nu_\tau$ mass measurement. The limiting mass sensitivity is directly proportional to $\sigma_p/p$. The design performance represents an improvement by a factor of 5 relative to Mark III and will result in 1 MeV/c$^2$ mass sensitivity. Many other experiments will benefit from such a precise momentum measurement; in particular there will be a significant improvement in the mass resolutions of both beam-unconstrained and beam-constrained decays.

2. *Photons.* A substantial improvement in the detection efficiency and resolution of events involving neutrals ($\gamma, \pi^0, \eta$ etc.) is seen when comparing a crystal electromagnetic calorimeter with other techniques. Some examples are shown in Figures 1 and 2. Note in Figure 1 that an improved energy resolution both sharpens the reconstructed $D$ mass *and* reduces the level of background (since tighter cuts can be made on $\pi^0$ and $\eta$ candidates). A high resolution and efficient electromagnetic calorimeter

| Experiment | Detector emphasis | | | | |
|---|---|---|---|---|---|
| | Charged particles | Photons | $\pi Kp$ i.d. | $e\mu$ i.d. | Hermeticity |
| $\tau$ physics: | | | | | |
| $\nu_\tau$, $\tau$ masses | • | • | • | • | • |
| $\tau \to l\nu_l\nu_\tau$ spectra | | • | | • | • |
| Precise branching ratios | | • | • | • | • |
| Second class currents | | • | | • | • |
| Weak hadronic current | • | • | • | • | • |
| $\tau$ electric dipole moment | | • | • | • | • |
| Rare decays | • | • | • | • | • |
| $D, D_s$ physics: | | | | | |
| $V_{cs}, V_{cd}$ (semileptonic decays) | | • | • | • | • |
| $f_D$ (pure leptonic decays) | | • | | • | • |
| Hadronic decays (CA, CS, DCS) | • | • | • | | |
| $D^o\bar{D}^o$ mixing, CP violation | • | | • | • | • |
| Rare decays | • | | | • | • |
| $J/\psi(3.10)$, $\psi'(3.69)$ physics: | | | | | |
| Spectroscopy ($c\bar{c}$, gg, hybrid, uds) | • | • | • | | |
| Rare decays | | • | • | • | • |

Table 1: Special detector requirements for individual $\tau$cF experiments. The presence of '•' signifies that the experiment requires special emphasis on this feature of the detector. In this context,'special emphasis' implies a performance that is substantially better than Mark III.

is necessary in order to single-tag $\tau^+\tau^-$ events with the $l + E_{miss}$ signature[2]; without such a calorimeter, the detector would lack sufficient resolution and hermeticity to isolate the events containing $\nu$'s.

3. $\pi, K, p$ *identification.* Hadronic particle identification is especially important in $D$ studies since it tags the $c$ or $\bar{c}$ flavour. It will also allow experimental tests to be made of the precise nature of $\tau$ decays in comparison with the predictions of the Standard Model. Finally, it is important in the studies of spectroscopy in $J/\psi(3.10)$ decays and of the charged weak current in $\tau$ decays.

4. $e, \mu$ *identification and hermeticity.* These aspects are important in almost all $\tau$cF experiments. The $\tau$cF detector aims to go beyond the traditional detection of charged leptons, by including neutral lepton tagging in a hermetic apparatus.

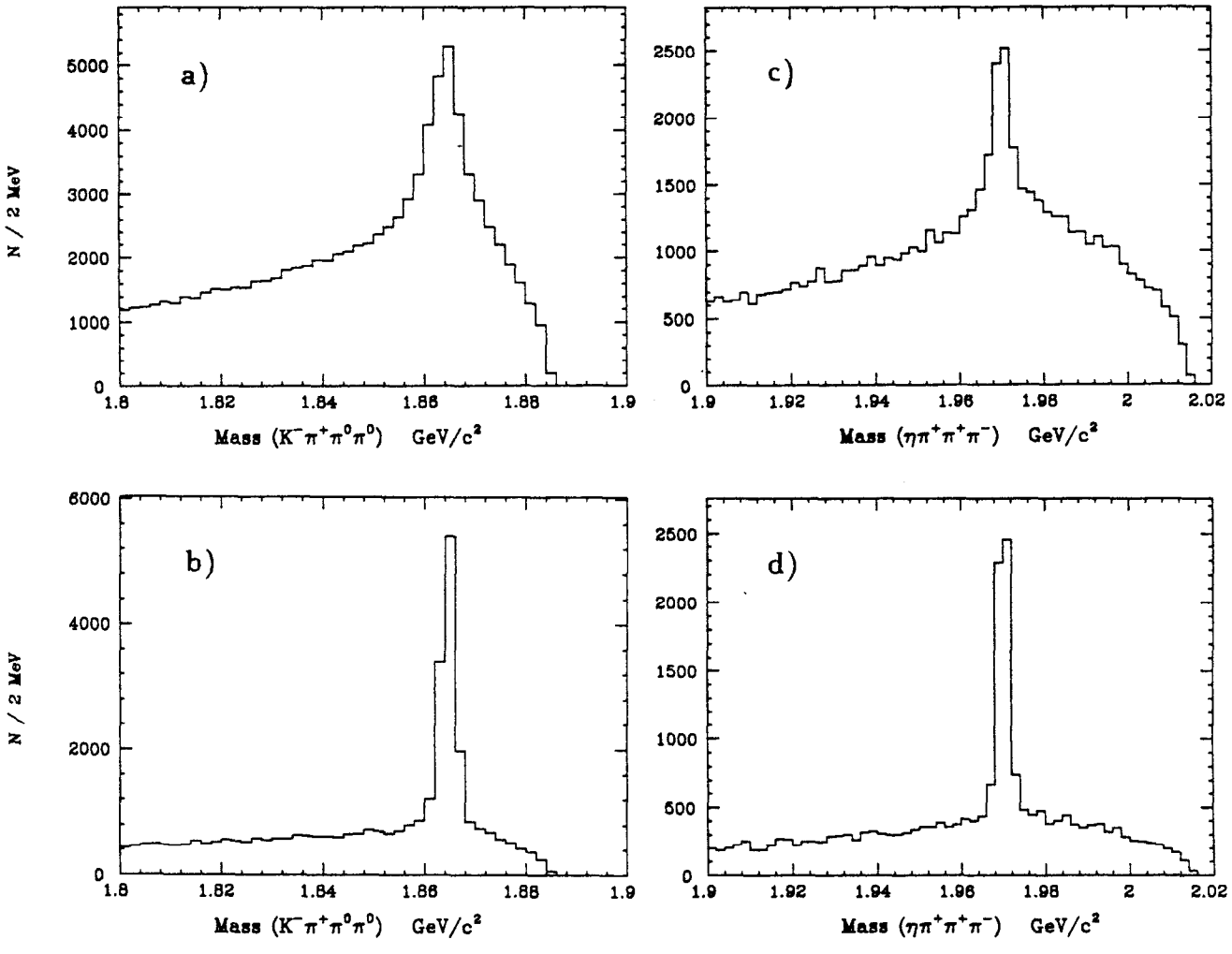


Figure 1: The effect of improved $\gamma$ energy resolution on tagging $D$ and $D_s$ decays that involve neutral particles[6]. Curves a) and c) correspond to $8\%/\sqrt{E}$ energy resolution, whereas b) and d) correspond to $2\%/\sqrt{E}$. All curves assume the same detection efficiency, which reaches 50% at 50 MeV [pessimistic for the crystal calorimeter curves b) and d)]. Reconstructed masses are shown for: a) and b) $D^0 \to K^-\pi^-\pi^0\pi^0$; and, c) and d) $D_s \to \eta\pi^+\pi^+\pi^-$, where $\eta \to \gamma\gamma$.

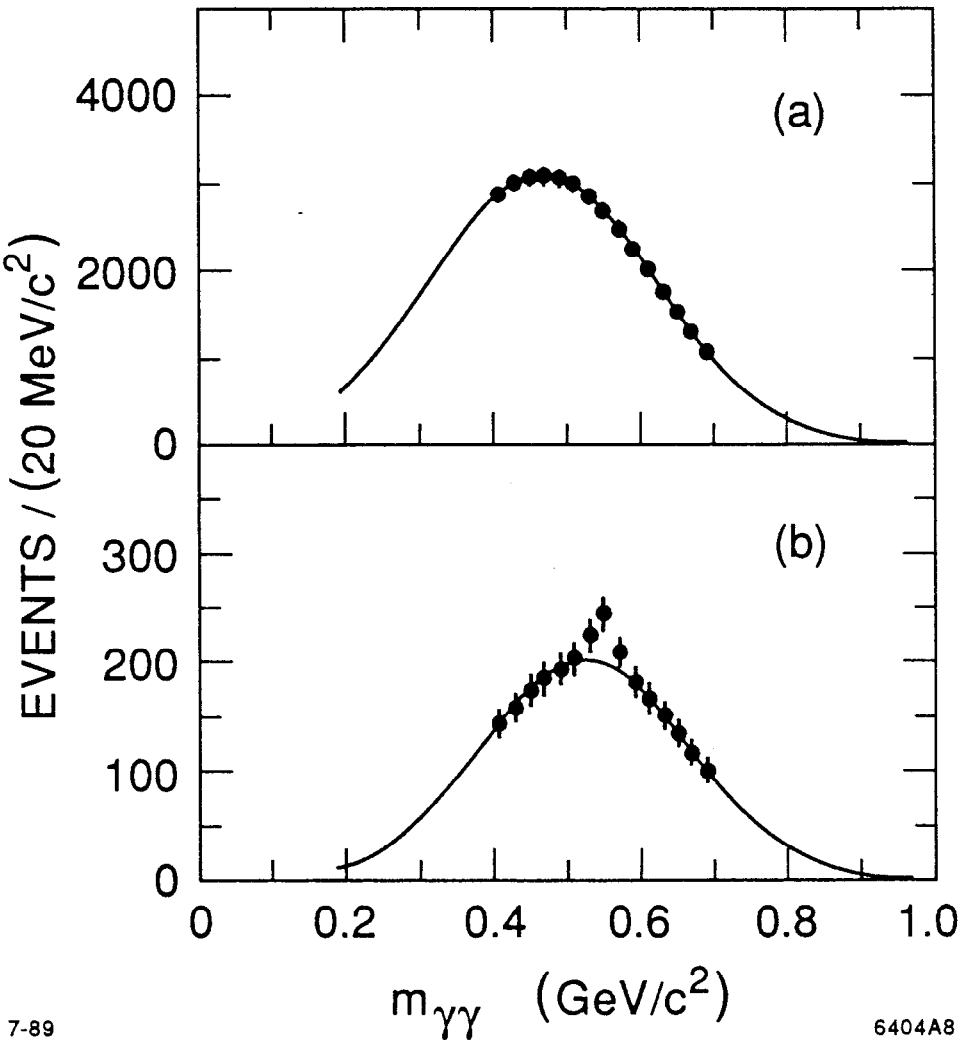


Figure 2: The effect of improved $\gamma$ energy resolution and detection efficiency on the search for the rare (br 1.5 $10^{-5}$) decay $\tau^- \rightarrow \pi^-\eta\nu_\tau$[7]. The curves show the $\gamma\gamma$ mass spectrum of the candidate events in a detector with: a) a sampling electromagnetic calorimeter with $8\%/\sqrt{E}$ energy resolution and a detection efficiency of 50% at 50 MeV; and, b) a crystal electromagnetic calorimeter with $2\%/\sqrt{E}$ energy resolution and a detection efficiency of 50% at 10 MeV.

| Measurement precision, $\sigma$ ($\mu$m) | $L_{DC}$ (m) | $B$ (T) | $1/X_0$ (rad. len. per m) | $p_t^{loop}$ (MeV/c) |
|---|---|---|---|---|
| 100 | 1.00 | 0.21 | $1.4\ 10^{-4}$ | 33 |
| | 0.80 | 0.38 | $3.3\ 10^{-4}$ | 45 |
| | 0.60 | 0.78 | $11\ 10^{-4}$ | 70 |
| 200 | 1.00 | 0.43 | $5.4\ 10^{-4}$ | 65 |
| | 0.80 | 0.76 | $13\ 10^{-4}$ | 91 |
| | 0.60 | 1.55 | $42\ 10^{-4}$ | 140 |
| 300 | 1.00 | 0.65 | $12\ 10^{-4}$ | 98 |
| | 0.80 | 1.14 | $30\ 10^{-4}$ | 140 |
| | 0.60 | 2.33 | $94\ 10^{-4}$ | 210 |

Table 2: Choices of the $B$ field and tracking detector lever arm $L_{DC}$ that meet the design performance for the momentum measurement: $[\sigma_p/p]^2 = [0.4\%p(\mathrm{GeV/c})]^2 + [0.3\%/\beta]^2$. Also indicated are the maximum allowable DC material $1/X_0$, and the limiting momenta of tracks that loop inside the DC, $p_t^{loop}$.

# 3 Detector dimensions

## 3.1 Choice of $B$ field and tracking detector lever-arm

The starting point in the design of the $\tau$cF detector is to define the tracking detector and its dimensions, and the required magnetic field. At the outset it was agreed that the appropriate device is a drift chamber (DC) in a solenoidal magnetic field. Other tracking detectors cannot meet the stringent low mass requirements. A TPC, for example, has massive walls and, moreover, is too slow for the high rate environment of the $\tau$cF, where the beam crossing period is 52 ns.

The detailed considerations of the central tracking design are given elsewhere in these Proceedings[8] and so we shall present here only the salient points. Values of $B$ and lever-arm $L_{DC}$ were calculated that satisfied the measurement precision term, $\sigma_p/p = 0.4\%p(\mathrm{GeV/c})$. In these calculations, a radial hit density of 1 cm$^{-1}$ was assumed, i.e. 100 hits per track for $L_{DC} = 1$ m. Three different values were taken for the measurement precision per hit: $\sigma = 100$, 200 and 300 $\mu$m. Having determined $B$ and $L_{DC}$ in this way, the (maximum) allowable material $1/X_0$ (rad.len. per m) that satisfied the multiple Coulomb scattering term, $\sigma_p/p = 0.3\%/\beta$, was calculated. The results are shown in Table 2, along with the corresponding limiting momenta of particles that will loop inside the DC, $p_t^{loop}$.

Note from Table 2 that relaxation of the mass requirement is most readily achieved by going to higher $B$ fields rather than by increasing $L_{DC}$. This reflects the multiple Coulomb scattering term, $\sigma_p/p \propto 1/(B\sqrt{L_{DC}})$, which improves relatively slowly with increasing $L_{DC}$. Finally, in order to have the minimum $p_t^{loop}$, the lowest value of $BL_{DC}$ that meets the $\sigma_p/p$ requirements should be selected.

The conclusions from Table 2 are as follows:

- There is a broad range of choices of $B$ and $L_{DC}$ that satisfy the measurement precision

term, $\sigma_p/p = 0.4\%p(\mathrm{GeV/c})$. Furthermore, the measurement precision per hit is not critical; $\sigma = 200$ $\mu$m is adequate to achieve the desired $\sigma_p/p$.

- The multiple Coulomb scattering term, $\sigma_p/p = 0.3\%/\beta$, places severe constraints on the amount of material that can be tolerated in the DC. For comparison, the radiation lengths per m of some DC gases at STP (0°C, 1 atm.) are: Ar(91 $10^{-4}$), $C_4H_{10}$(59 $10^{-4}$), $CO_2$(55 $10^{-4}$), $C_3H_8$(44 $10^{-4}$), $CH_4$(15 $10^{-4}$) and He(1.9 $10^{-4}$). Wires, in addition, contribute substantially to the overall DC material, e.g. in the case of the Mark II DC, the wires represent 74 $10^{-4}$ rad. len. per m.

  In order to achieve the lowest possible material, it is planned[9] to use a He-based DC gas, such as 94% He : 6% $C_3H_8$ ($1/X_0 = 5\,10^{-4}$ rad. len. per m). Furthermore, with the use of Al field wires and with suitable reduction in the number of wires, it is anticipated that the contribution from the wires can be reduced to 20 $10^{-4}$ rad. len. per m, resulting in a total DC material of 25 $10^{-4}$ rad. len. per m. With this amount of material, the design performance for $\sigma_p/p$ can be reached within the following range of values for the lever-arm and magnetic field:

$$L_{DC}(B) \;=\; 0.60\mathrm{m}(1.5\mathrm{T}) \rightarrow 0.80\mathrm{m}(1.1\mathrm{T})$$

- The resulting momentum of 'trapped' particles is $p_t^{loop} = 140$ MeV.

## 3.2 Influence of electromagnetic calorimeter on detector size

The major influence of the electromagnetic calorimeter on the detector dimensions is due to its cost. Figure 3 shows the cost of the crystals for a $16X_0$ calorimeter of CsI, which has a relatively low price (\$2 cm$^{-3}$, for large purchases) amongst crystal scintillators. This Figure demonstrates a sharp rise in the cost with increasing radius of the electromagnetic calorimeter. A subjective financial limit is reached at an inner radius of approximately 1 m. It is apparent that the cost of the electromagnetic calorimeter will constitute a large fraction ($\geq 50\%$) of the total cost of the detector and that substantial savings will result from minimizing its inner radius, subject to maintaining adequate $\gamma$ angular resolution. This militates in favour of choosing a high $B$ field and low $L_{DC}$. Finally, both cost and performance dictate that the electromagnetic calorimeter be located *inside* the detector solenoid.

# 4 Design concept

## 4.1 Basic configuration

Following the previous considerations, we arrive at the basic configuration for the $\tau$cF detector (Figures 4 and 5). The dimensions in this figure and in the following discussion should be considered as approximate, although they are probably within 15% of the optimized values. A brief initial specification of each component is as follows:

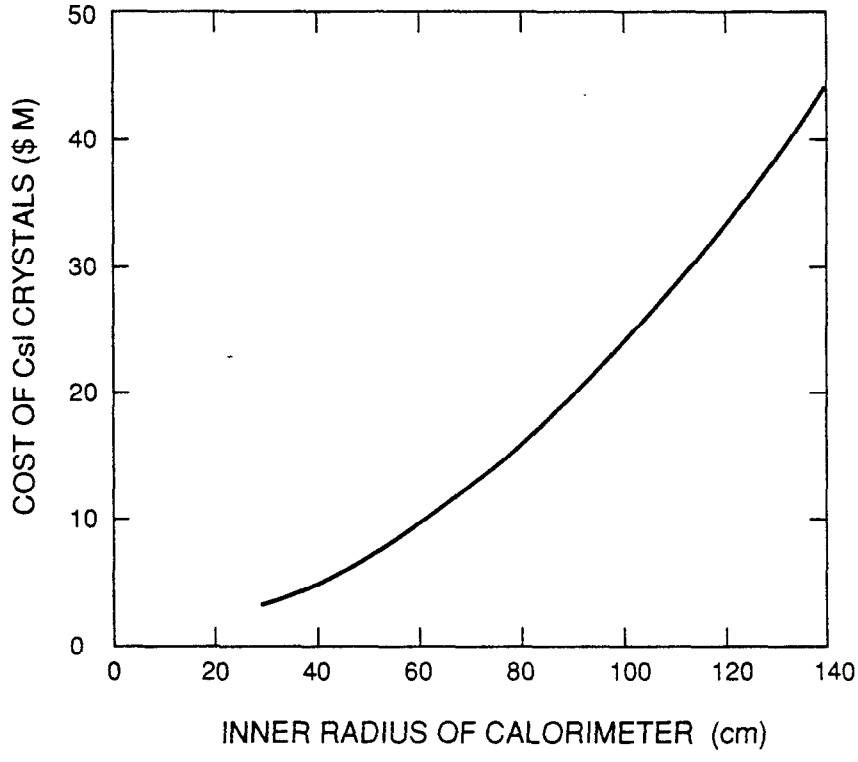


Figure 3: The cost of the crystals for a $16X_0$ CsI electromagnetic calorimeter vs. the inner radius of the calorimeter. The design criteria $\Omega$(barrel) = 90% x $4\pi$ str. is assumed.

- **Magnet.** Given the requirement of a field strength in the range $1 \rightarrow 1.5$ T and the extended operation forseen for the $\tau$cF (10 months per year for a period of 10 or more years), the optimum choice for the solenoid is a superconducting, rather than warm, coil. The dimensions of the cryostat are: inner diameter 2.7 m, outer diameter 3.2 m, and length 5 m. With 1.5 T field, the stored energy is 160 MJ. The perpendicular thickness of the coil and cryostat is 0.9 rad.len. (0.20 $\lambda_{abs}$).

- **Tracking detector.** Since the free space between the micro-beta ($\mu\beta$) quadrupole magnets (0.20 m outer radius) is only 1.60 m, they project inside the volume of the tracking detector. In order to accommodate this constraint, the wires taper to shorter lengths as they approach the interaction point. This has the advantages of creating useful space for small-angle detectors and their readout, reducing the dc current on the innermost wires, and providing a trigger with natural selection of events from the z region near the interaction point.

  Depending on the strength of the magnetic field, the tracking detector extends to an outer radius of 70-90 cm, with a hit density of 1 per cm. The wire lengths are 3.6 m or less. Measurement of the z coordinate is done by narrow-angle stereo since this is compatible with the low-gain requirements of $dE/dx$ measurements.

  The He-based drift gas will result in a reduced precision of both position and $dE/dx$. This is due to the small deposition of ionization (6 ion pairs per cm in He, compared

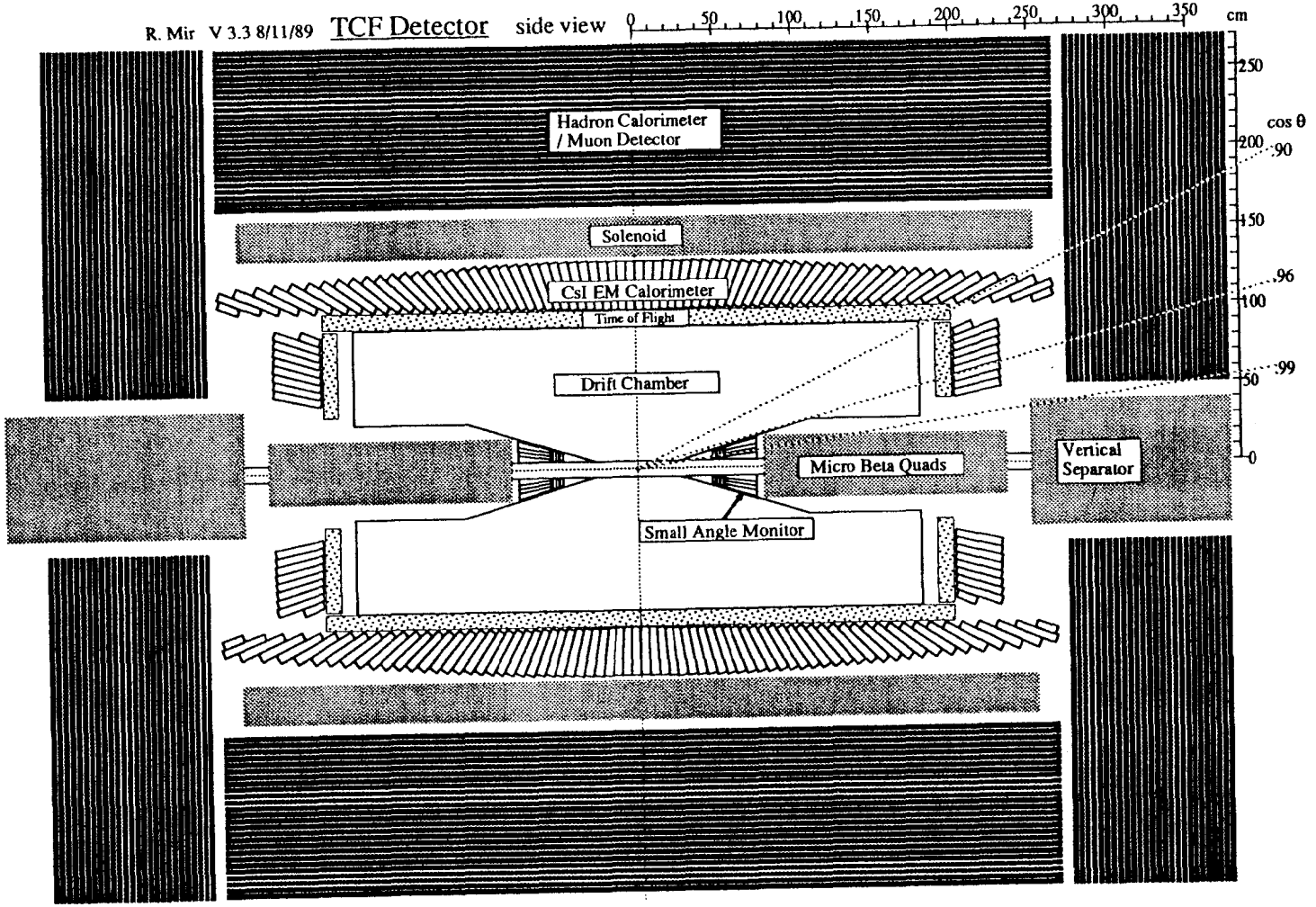


Figure 4: The basic configuration of the $\tau$cF detector (side view). The primary rôle of the hadron calorimeter is to tag the presence of $K_L^0/n$, and not the traditional one of hadron energy measurement.

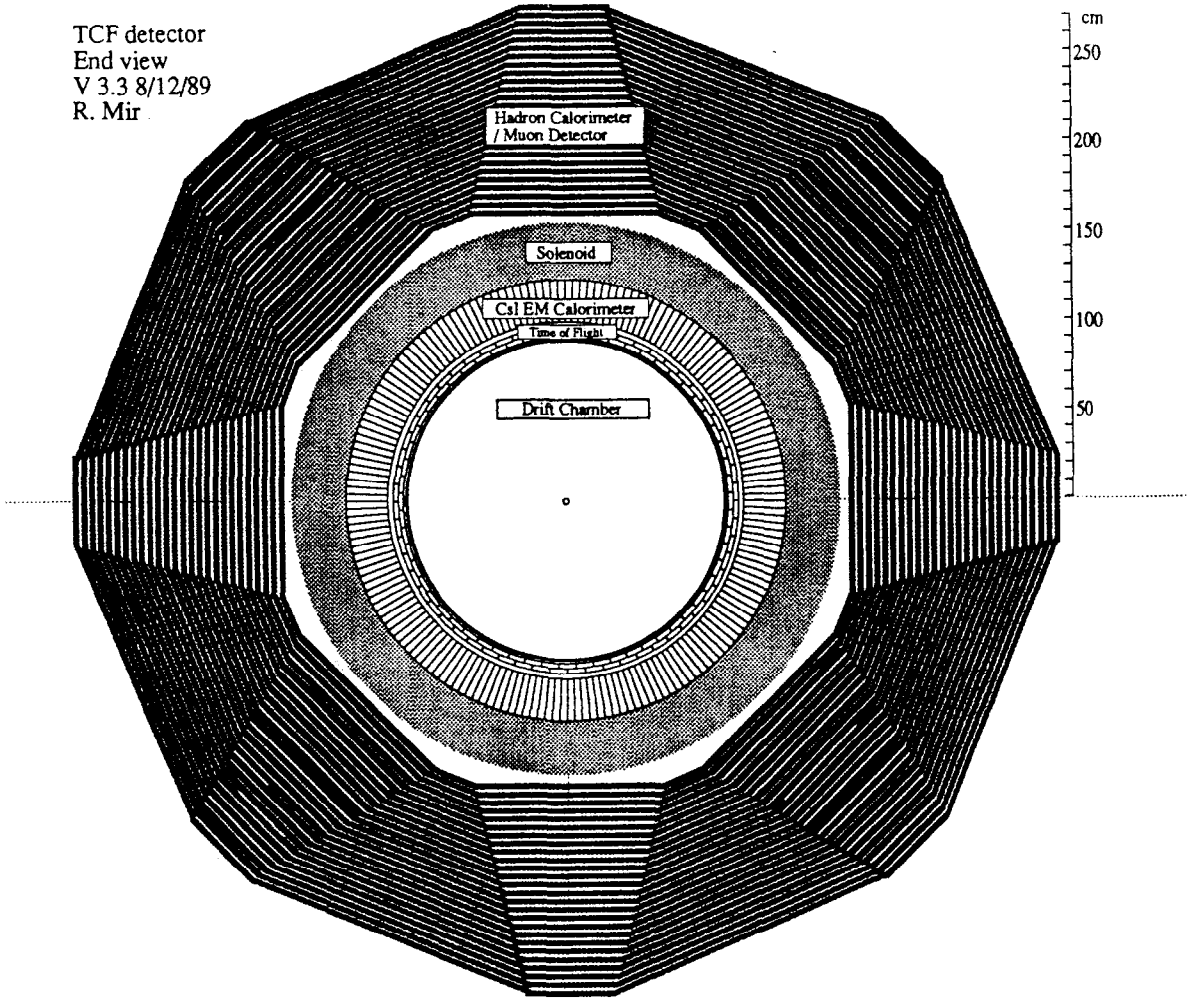


Figure 5: The basic configuration of the τcF detector (end view).

with e.g. 29 per cm in Ar). However, neither of these disadvantages is too serious. An advantage of this gas, in addition to superior momentum measurenment at low energies, is a relatively small cross-section for synchrotron X-rays ($\sigma \propto Z^4$), which are potentially a major background source in tracking detectors at high-current $e^+e^-$ storage rings.

The inner region of the tracking detector ($5 \leq r \leq 20$ cm) is forseen as a precise drift chamber, whose functions are to measure accurately the track positions and angles close to the vertex, and to improve the measurement of tracks that emerge at small polar angles. This device has a close wire spacing and perhaps a different gas than the He-$C_3H_8$ of the central tracker. In this case, a thin membrane would separate the two gas volumes. The inner tracking detector uses the (0.8 mm thick) Be vacuum chamber as a spool piece for supporting the wire tension; the central tracker wire

tension is carried by a thin outer cylinder.

Following the design specifications, the tracking detector has an extended barrel region that subtends 90% x $4\pi$ str., leaving small end-caps that cover 6% x $4\pi$ str. The inner face of each $\mu\beta$ quad is also instrumented, as described below, to bring the total detector coverage to 99.7% x $4\pi$ str.

- **Electromagnetic calorimeter.** Among the candidate materials for the calorimeter, probably CsI(Tl) represents the best choice. The advantages are as follows: acceptable cost, large light yield (52 photons per keV, which results in good $\gamma$ measurement at low energy; the photodiode equivalent noise is 0.6 MeV), easy handling, and a reasonably short radiation length $X_0 = 1.86$ cm. The disadvantages are poor radiation hardness and slow light emission ($\tau \approx 900$ ns, with long tails; 5% of the light appears after 3 ms). However, both these disadvantages can be overcome with suitable precautions. Other choices that are under study include pure CsI, and $BaF_2$, both of which have faster light emission than CsI(Tl). The calorimeter is arranged in a tower geometry that projects, with a small offset, towards the interaction point. This will eliminate blind regions of the calorimeter and ensure the detector is hermetic. Each crystal is $16X_0$ in depth and has an entrance face $\approx 5$ x 5 cm$^2$. Each tower is read out with a photodiode/ waveshifter-plate mounted on the rear face.

  Two novel features of the calorimeter were discussed. The first is an additional diode that reads out the front face of each tower, thereby providing depth information to aid $e\pi$ separation. The second involves a position-measuring layer situated after 3-4 $X_0$. One possibility is to install a superlayer of scintillating plastic fibres, arranged in a zuv geometry and read out via an image intensifier/ CCD system. An alternative possibility is a layer of Si pads or strips. In addition to improving the $\gamma$ angular accuracy, this layer would give timing information that would provide a strong rejection of photon backgrounds, such as those caused by neutron albedo from hadron interactions elsewhere in the detector.

- **Hadron calorimeter/ $\mu$ detector.** Situated outside the solenoid is a fine-grained hadron calorimeter whose functions are to tag the presence of $K_L^0/n$, to identify $\mu$, and to provide a flux return path. This has a depth of 80 cm Fe, made from 2.5 cm thick plates, separated by tracking chambers of 1.5 cm thickness. The best choice is probably drift chambers with long drift gaps (10-20 cm). Data from these chambers are continually recorded on a FADC and read out when a trigger occurs. Separation of $\pi/K$ from $\mu$ is achieved by a combination of precise range measurements and absence of interactions.

  The effect of the solenoid material on the performance of the hadron calorimeter is under study. It is not expected to be a problem since it is equivalent to a single plate of the calorimeter, and it occurs early in the $\mu$ range (300 MeV/c).

- **Time-of-flight (ToF) counters.** ToF counters are an important component of the trigger and particle identification. From the experience of CLEO II[10] and others, we expect a resolution of 120 ps is feasible. The newly-developed mesh phototubes

from Hamamatsu appear to be capable of reaching this performance while operating inside a strong magnetic field. Use of these tubes would eliminate the need for large light-pipe holes in the hadron calorimeter, which would simplify the construction and improve the hermeticity.

- **Small-angle detectors.** The inner face of each $\mu\beta$ quad is instrumented with an array of $16X_0$ BGO crystals, preceded by a tracking detector. These detectors complete the solid angular acceptance and provide the luminosity monitor. BGO is a good candidate due to its short radiation length (1.12 cm) and radiation hardness. The readout is identical with that of the central electromagnetic calorimeter. Another approach under consideration is a Si/W sampling calorimeter ($X_0$ = 8 mm) similar to the SLD design[11].

  It may also be possible to consider instrumenting the inner bore of the $\mu\beta$ quads with a Pb/scintillating fibre calorimeter of 1 cm radial thickness. This would result in essentially complete coverage of the solid angle and also provide an efficient tag of 2-photon events. No calculations were done to estimate the occupancy of this counter which, in order to be useful, must be below 0.1%.

The elements of the $\tau$cF detector are similar to CLEO II, which has just started operation at CESR. In consequence, most of the detector components are well understood and will require little R&D prior to final design. The main differences of the $\tau$cF detector with respect to CLEO II reflect an optimization for $\tau$-charm physics, notably: improvement of the momentum resolution at low energy, increase of the barrel solid angle, enhanced particle identification at low energies (described below), and hermeticity with a fine-grained outer hadron calorimeter/ $\mu$ identifier.

## 4.2 Configuration with improved particle identification

Most $\tau$-charm physics can be done with the particle identification capabilities of the basic $\tau$cF detector configuration. This demonstrates another advantage of operating close to $\tau$-charm threshold: the kinematic limit of particles from $\tau$ and $D$ decays is $\approx$ 1 GeV/c and so the identification of $\pi, K$ and $p$ is relatively easy using a combination of ToF and $dE/dx$.

The most stringent requirements on particle identification are made by the measurements of $D^o\bar{D}^o$ mixing and CP violation[12]. One important signature of mixing is $D^o\bar{D}^o \rightarrow (K^+\pi^-)_{D^0}(K^+\pi^-)_{\bar{D}^0}$ + cc. A fake signal can be generated if *both* the $K$ and the $\pi$ from a single $D^0$ are misidentified. The momenta of these particles are in the range 0.8 $\rightarrow$ 1.0 GeV/c where the separation relies purely on ToF. If we assume a 1% misidentification probability, then the fake rate will be $2\ 10^{-4}$, which constitutes the limiting experimental sensitivity to a mixing signal. These experiments will also use semileptonic decays to tag the charm flavour in a study of the charge composition of dilepton decays. Since there is a four-fold increase in data if both $\mu$ and $e$ can be used ($ee$, $e\mu$ and $\mu\mu$), $\mu$ detection is worth a special effort.

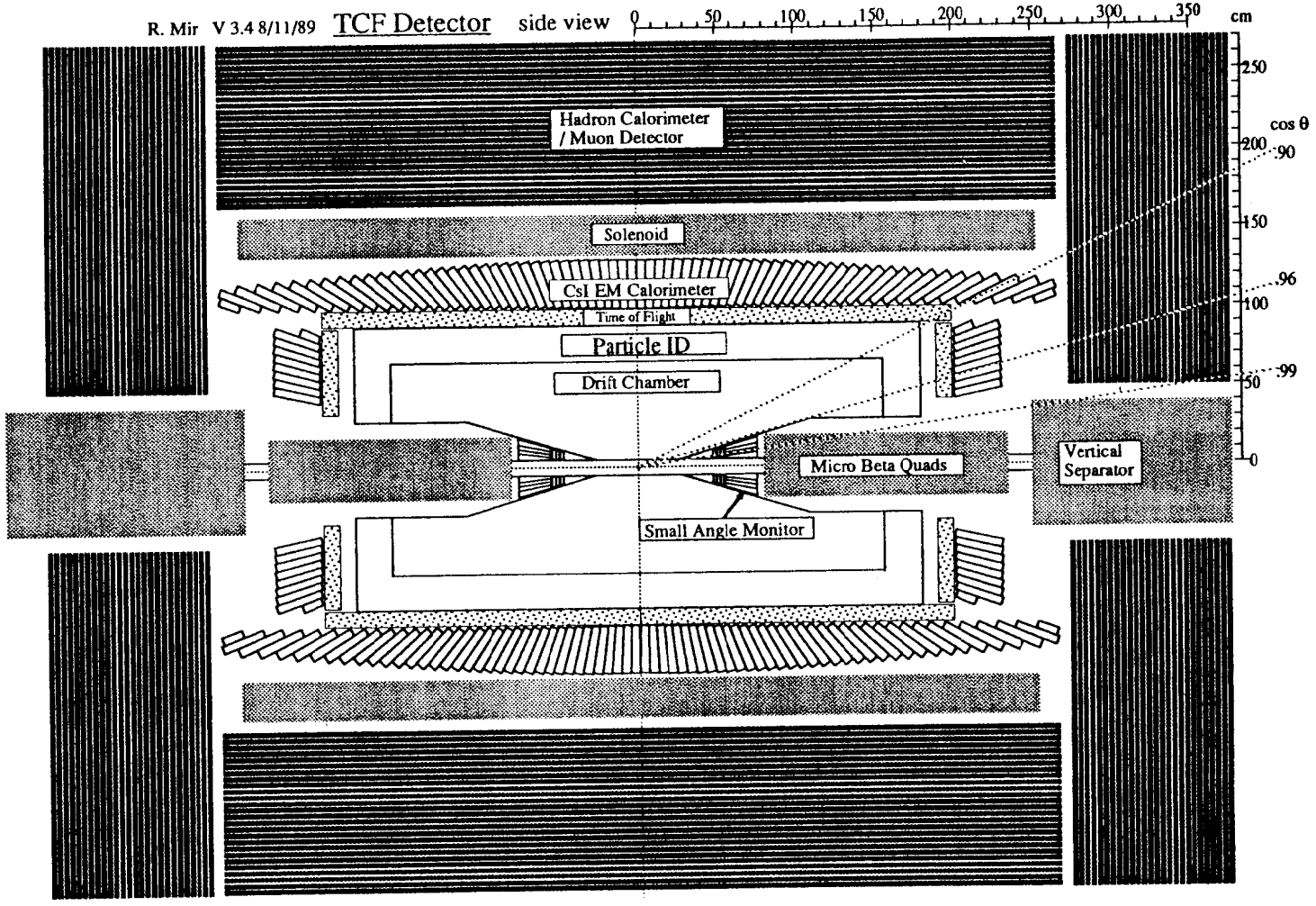


Figure 6: A modified version of the $\tau$cF detector with improved particle identification (side view). A space of approximately 20 cm is reserved between the drift chamber and the time-of-flight counters for a particle identifier. The dimensions of this version of the $\tau$cF detector with respect to the basic configuration are unchanged except for a reduction in the outer radius of the drift chamber. In order to maintain the design $\sigma_p/p$, there is a corresponding increase of the $B$ field.

In view of experiments such as these, which require extremely clean particle tagging, we investigated a $\tau$cF detector configuration with enhanced particle identification (Figure 6). The idea is to introduce an additional detector layer that will both reduce the overall misidentification probability and provide some redundancy, so that the validity of a signal can be internally verified. A 20 cm space between the central tracking chamber and the ToF counters is sufficient for several options, such as a dedicated $dE/dx$ device, improved ToF or a Cerenkov Ring Imaging Device (CRID).

The most serious tradeoff in this scheme is the introduction of material (up to 20% rad. len.) in front of the electromagnetic calorimeter. This would result in deterioration of the energy resolution of $\approx$ 20% of the photons (those which converted before the calorimeter). There would also be a reduction in the detection efficiency of photons at the lowest energies, e.g. 20% reduction at 10 MeV. However, as indicated in Table 1, reduced photon peformance would be not be a problem for certain experiments, such as $D^o\bar{D}^o$ mixing and CP violation. In others, where photon detection is crucial, the particle identifier could be removed and the $\tau$cF detector operated with either an empty gap or an additional, low mass, tracking detector.

The differences in cost and performance of the two designs, with an empty gap in the second, are probably not significant. However, the second design has the important advantage of the potential to upgrade the particle identification. Flexibility for upgrades is an important consideration in large expensive detectors such as this, which are forseen to have a long ($\geq$ 10 year) lifetime. This flexibility must be factored into the detector design at the outset.

The particle identifier may be based on present techniques or even future ones that could develop during the lifetime of the detector. Some of the present options are discussed below.

### 4.2.1 $dE/dx$ in gaseous detectors

The $dE/dx$ particle separation in CLEO II is shown in Figure 7. This Figure illustrates how useful are $dE/dx$ measurements to particle separation in the low-$\beta$ region. Calculations[13] of the performance of He-$C_3H_8$ gas in the $\tau$cF detector (Figure 8a) indicate a performance close to that of CLEO II. We also find (Figure 8b) that a dedicated $dE/dx$ particle identifier of 20 cm depth has almost equal performance. The combination of the $dE/dx$ information from both devices will provide $3\sigma$ $\pi K$ separation up to 800 MeV/c. Useful hadron-electron separation is also provided, as shown in Figure 9.

### 4.2.2 Time-of-flight

The $\pi K$ separation by ToF in the Mark III detector is illustrated in Figure 10. Particle separation by ToF is a relatively simple technique that has been highly successful at low energies, and there is a clear case to provide the $\tau$cF detector with the best possible timing resolution. The $\pi K$ separation by ToF is shown in Figure 11[14]. In the $\tau$cF detector, the barrel ToF counters are located at a radius $\approx$ 95 cm. Useful separation at 1 GeV/c therefore requires a timing resolution of 120 ps which, as discussed above, may be

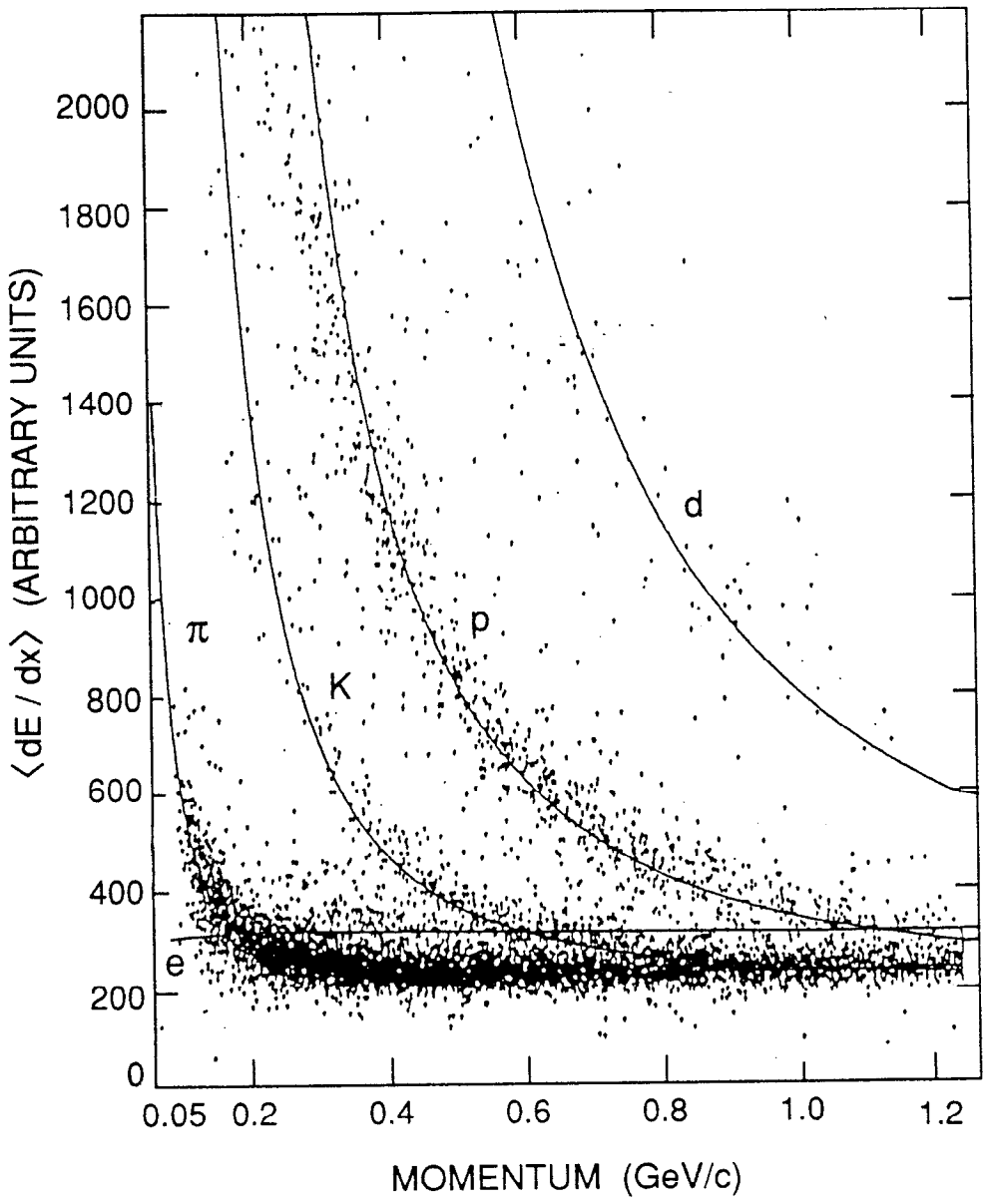


Figure 7: Mean energy loss in the CLEO II drift chamber [1 atm. Ar-$C_2H_6$, 72 cm, 51 samples, $(dE/dx)_{FWHM} = 14\%$]. The $dE/dx$ resolution in the $\tau$cF detector is expected to be similar to these data.

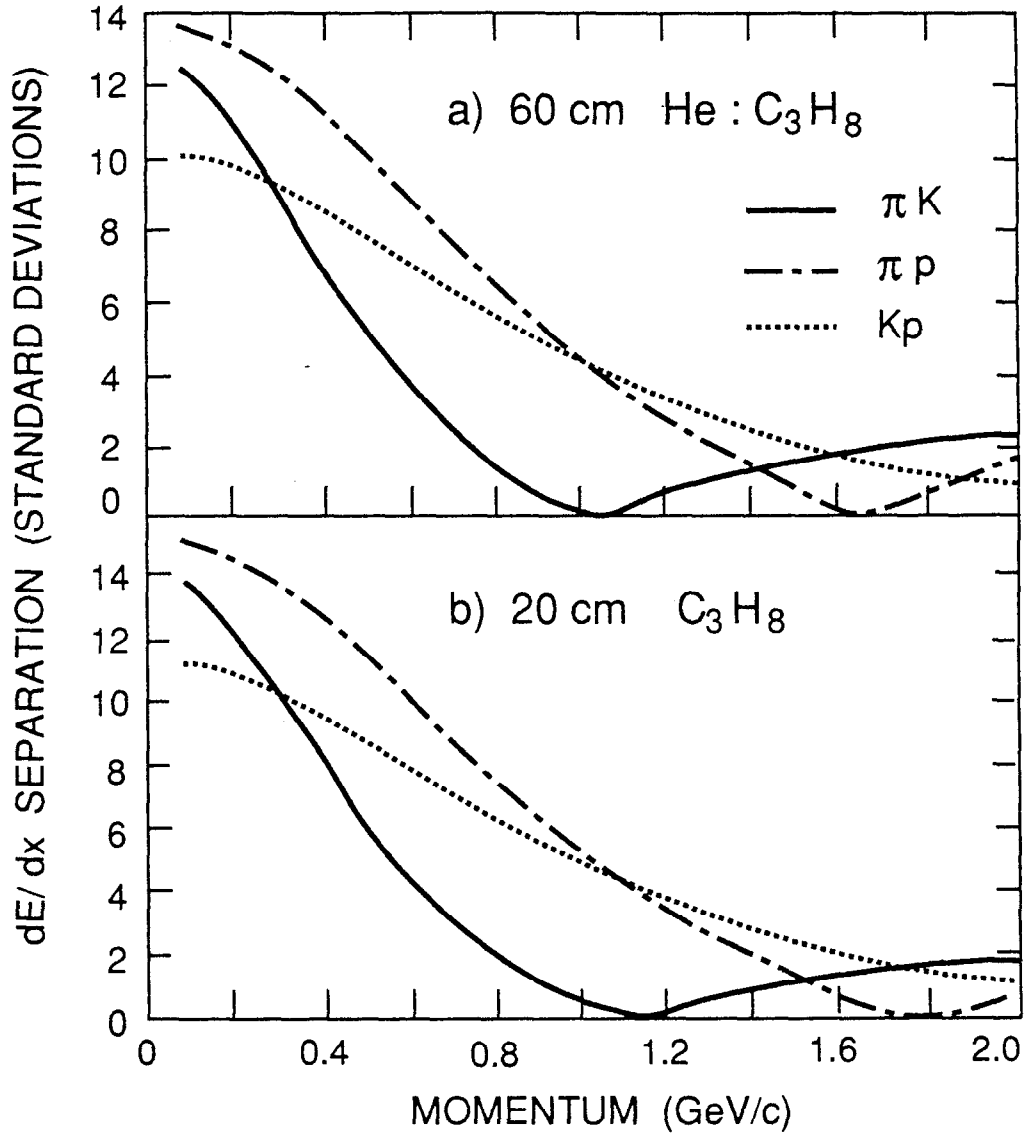


Figure 8: $dE/dx$ hadron-hadron separation in the $\tau$cF detector: a) central tracking chamber (1 atm 93.8%:6.2% He-$C_3H_8$, 1 cm per sample, 60 samples); and, b) dedicated particle identifier (1 atm $C_3H_8$, 1 cm per sample, 20 samples).

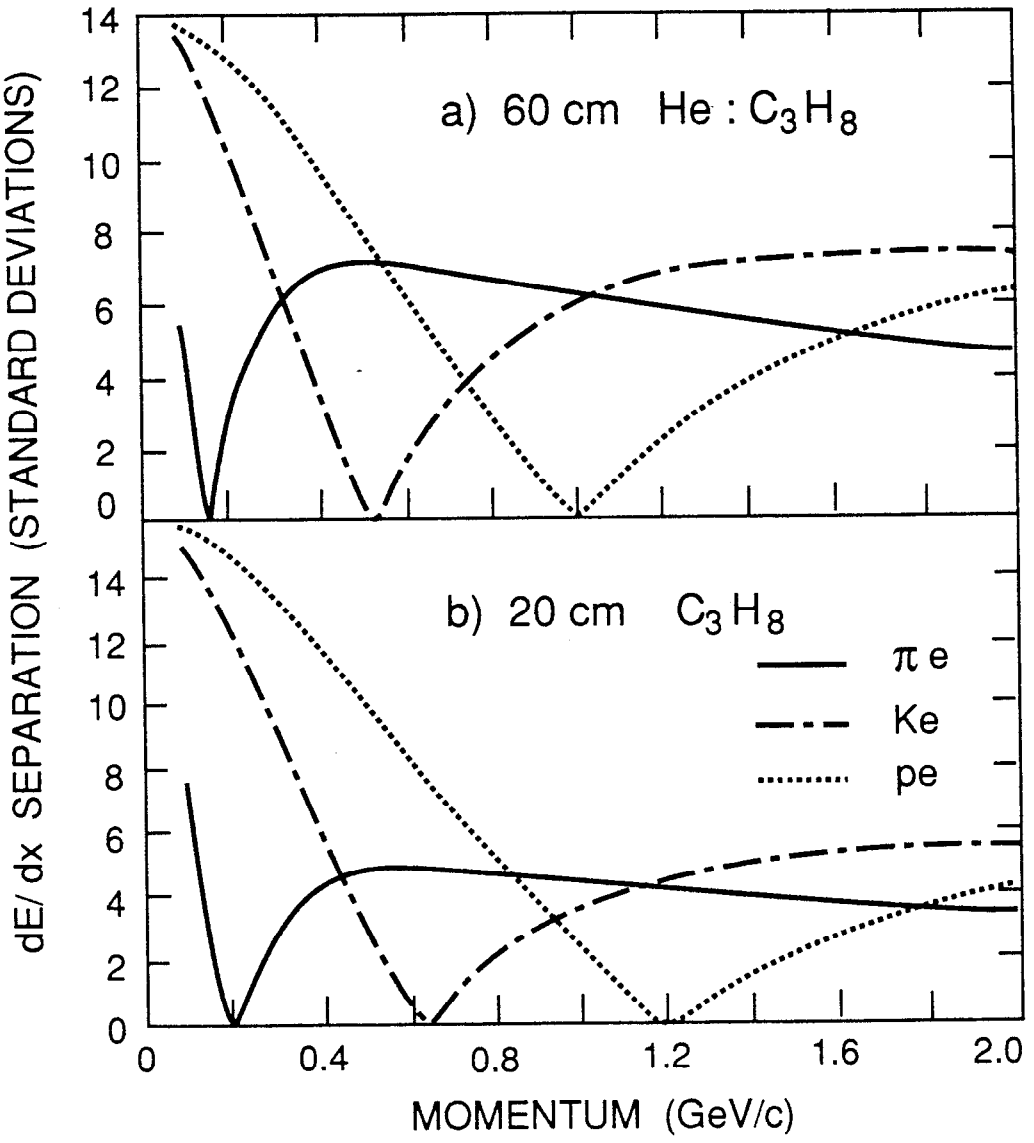


Figure 9: $dE/dx$ hadron-electron separation in the $\tau$cF detector: a) central tracking chamber (1 atm 93.8%:6.2% He-$C_3H_8$, 1 cm per sample, 60 samples); and, b) dedicated particle identifier (1 atm $C_3H_8$, 1 cm per sample, 20 samples).

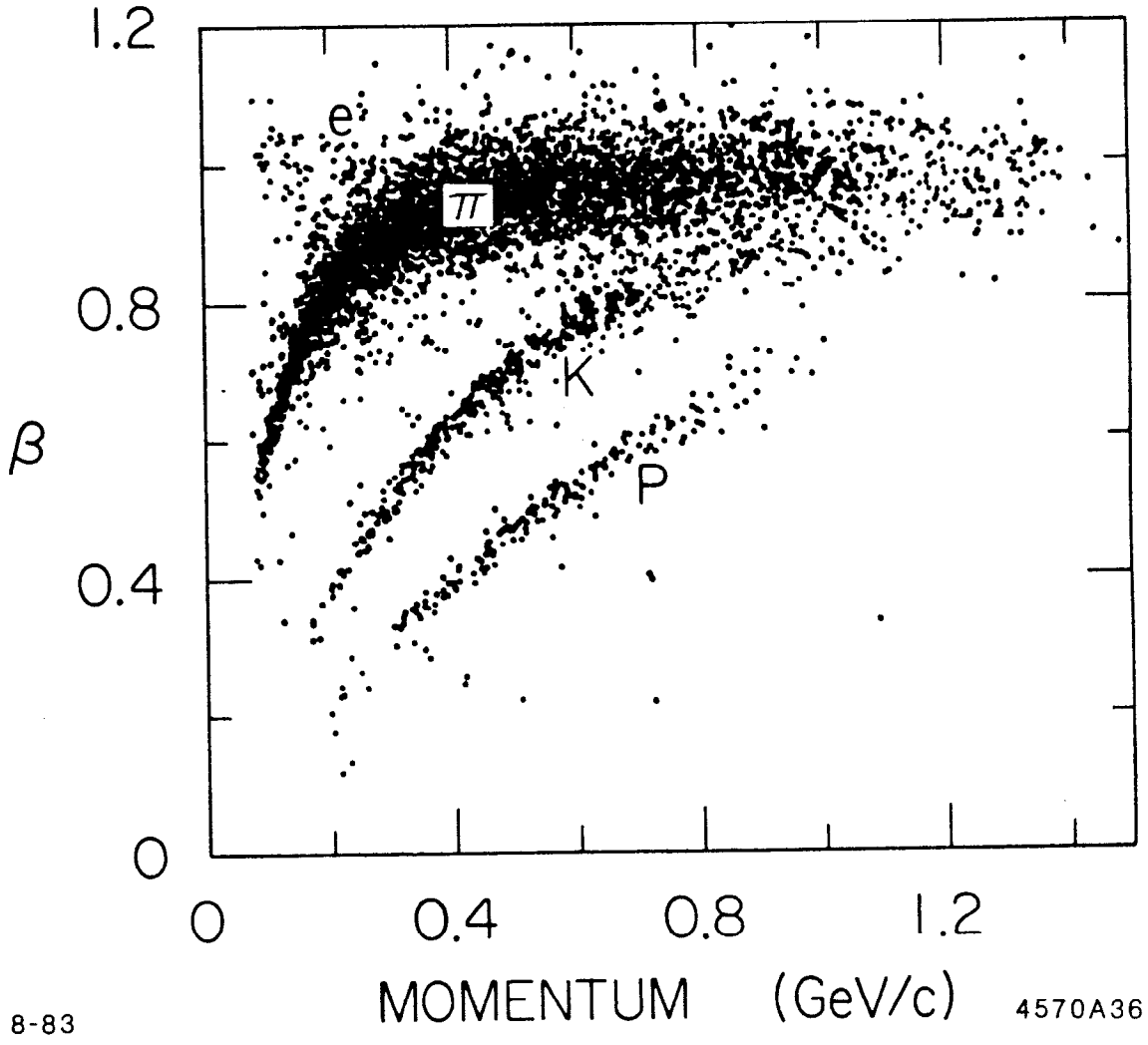


Figure 10: Time-of-flight particle separation in the Mark III detector at SPEAR ($\sigma_{ToF}$ = 175 ps and minimum flight path = 1.2 m).

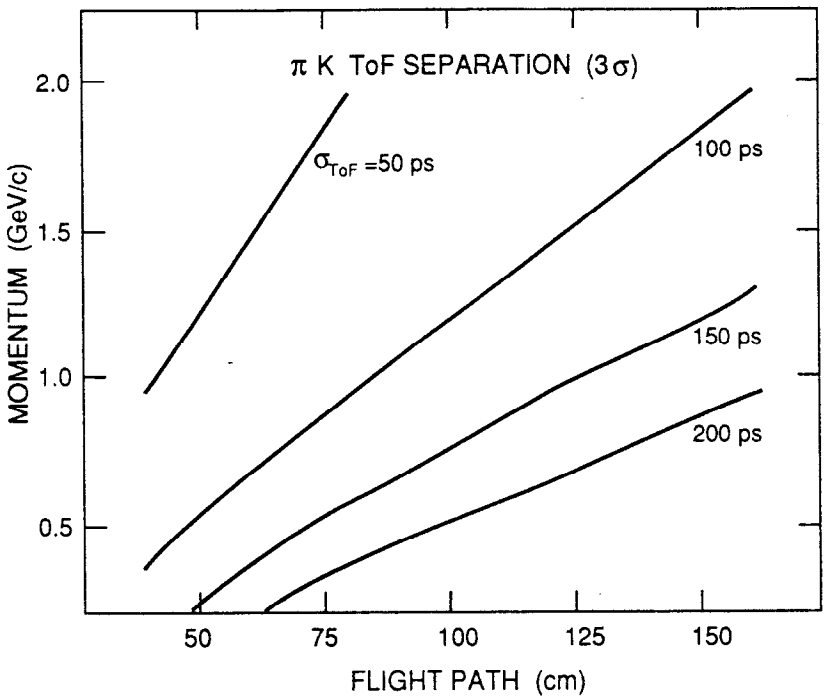


Figure 11: $\pi K$ separation ($3\sigma$ limits) by time of flight. Each curve corresponds to a different $\sigma_{ToF}$, as indicated.

achievable with plastic scintillation counters of thickness 5 cm (12% rad. len.). The effects of energy loss in this material on the resolution of the electromagnetic calorimeter can be largely compensated by adding the energies measured in the individual ToF counters to the corresponding energies seen in the calorimeter.

### 4.2.3 Cerenkov ring imaging

A CRID with a liquid freon ($C_6F_{14}$) radiator is well-suited to particle identification in this energy range, as demonstrated in Figure 12[15]. This device would eliminate the difficulties in $\pi K$ separation near 1 GeV/c. Moreover a CRID has excellent $e\pi$ and $\mu\pi$ separation at these energies. In particular it can provide strong $\mu\pi$ separation in the difficult low momentum region. As discussed above, the disadvantage is the large material: $\approx$ 20% rad.len. With the startup of the large Cerenkov ring imaging detectors of DELPHI and the SLD, we will soon be able to see how well these detectors meet their promised high performances for particle identification.

## 4.3 Performance summary

Finally, we summarize in Table 3 the performance of the $\tau$cF detector in comparison with Mark III (or, equivalently, with the BES detector at BEPC, which has a similar performance to Mark III).

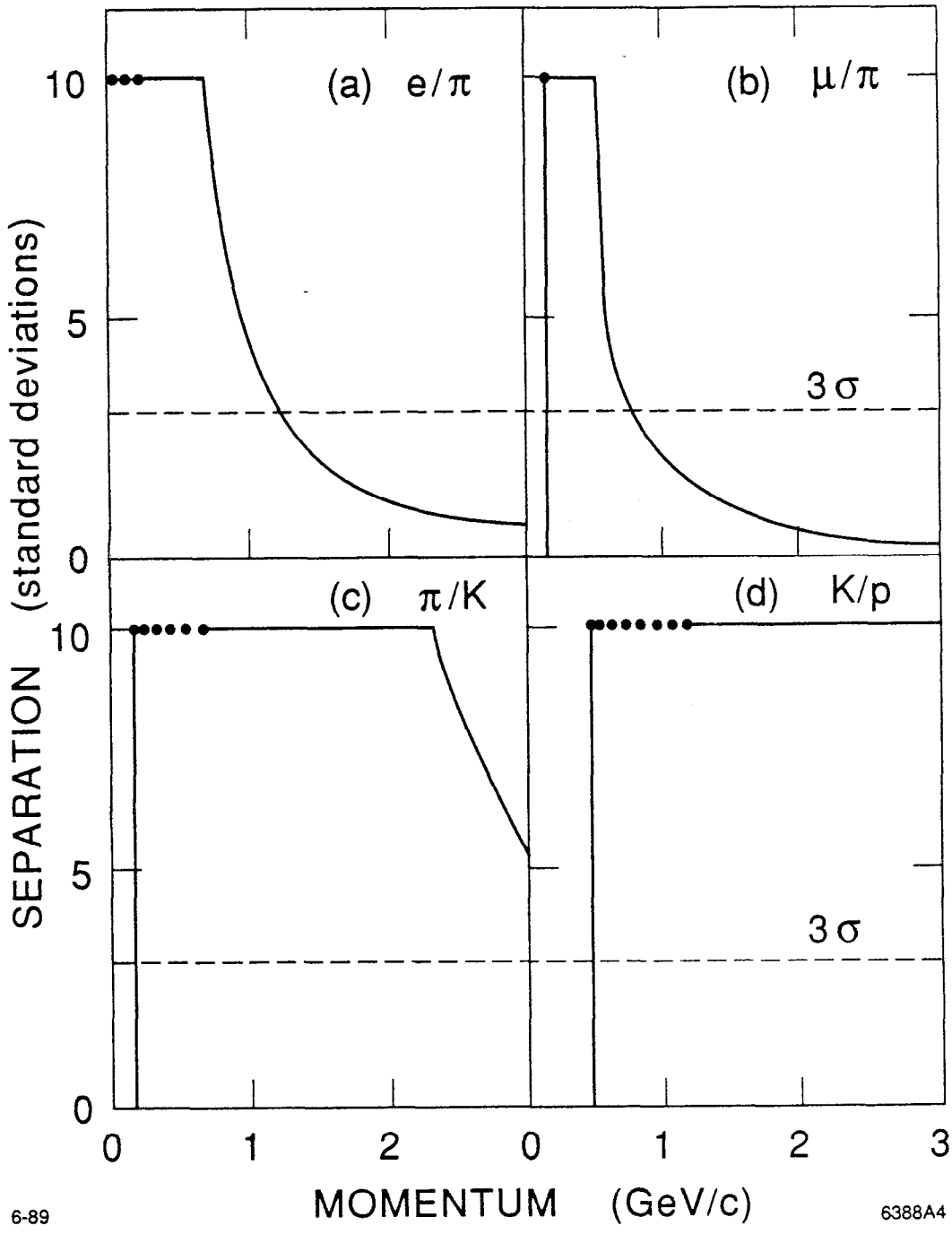


Figure 12: Particle separation in the CRID with a liquid freon ($C_6F_{14}$) radiator. The curves are considered to be saturated at $10\sigma$. The dots correspond to regions where only the lighter particle emits Cerenkov light (i.e. threshold-counter discrimination). The low momentum cutoffs correspond to insufficient light emission from the lighter particle, in either the liquid radiator or quartz windows, to provide reliable separation. The separation is shown for: a) $e\pi$; b) $\mu\pi$; c) $\pi K$; and d) $Kp$.

| | $\tau$cF | Mark III |
|---|---|---|
| Charged particles: | | |
| Momentum resolution $[\sigma_p/p(\mathrm{GeV/c})]^2$ | $[0.4\%p]^2 + [0.3\%/\beta]^2$ | $[1.5\%p]^2 + [1.5\%/\beta]^2$ |
| Angular resolution: $\sigma_\phi$ (mr) | 1 | 2 |
| $\sigma_\theta$ (mr) | 3 | 11 |
| Vertex precision: $[\sigma_{xy}(\mu\mathrm{m})]^2$ | $[40/p(\mathrm{GeV/c})]^2 + [50]^2$ | - |
| $\sigma_z$ (mm) | 1.5 | 15 |
| $p^\pi_{min}$(MeV/c) for efficient tracking | 50 | 80 |
| $\Omega$(barrel) (x4$\pi$ str.) | 90% | 70% |
| Photons: | | |
| Energy resolution $[\sigma_E/E(\mathrm{GeV})]^2$ | $[2\%/\sqrt{E}]^2 + [1\%]^2$ | $[18\%/\sqrt{E}]^2$ |
| Angular resolution $[\sigma_{\theta,\phi}$ (mr)$]^2$ | $[3/\sqrt{E}]^2 + [1]^2$ | $[10]^2$ |
| $2\gamma$ angular separation $\Delta\theta_{2\gamma}$ (mr) | 100 | 20 |
| $E^\gamma_{min}$(MeV) for efficient detection | 10 | 100 |
| Particle identification: | | |
| $h \to e$ rejection | $10^{-3} \to 10^{-5}$(+CRID) | 4% at 0.5 GeV/c |
| $h \to \mu$ rejection | $4\%/p(\mathrm{GeV/c})$ | 5% at 1.0 GeV/c |
| $\pi \to K$ rejection | $10^{-2} \to 10^{-4}$(+CRID) | $2\sigma$ at 1.2 GeV/c |
| $K^0_L/n$ detection efficiency | 95% | 62% |
| $E_{min}$(MeV) for efficient $\nu$ tagging | $\approx 100$ | - |

Table 3: Comparison of the performance of the $\tau$cF and Mark III detectors.

# 5 Conclusions

The conclusion from our studies is that a $\tau$-charm Factory detector that successfully meets the physics requirements can be built with present technologies. Our design is similar to CLEO II, which provides existence-proof of its feasibility. The main differences of the $\tau$cF detector with respect to CLEO II reflect an optimization for $\tau$-charm physics, notably: improvement of the momentum resolution at low energy, increase of the barrel solid angle, enhanced particle identification at low energies, and hermeticity with a fine-grained outer hadron calorimeter/$\mu$ identifier.

In addition to the basic configuration, a second design with improved particle identification was studied. This latter design includes space for a dedicated particle identifier which may be installed for certain experiments where particle identification is of primary concern. Both designs require further evaluation and optimization.

The performance of the $\tau$-charm Factory detector represents a substantial improvement in almost all respects relative to Mark III, but especially with regard to electromagnetic and hadronic calorimetry. This detector, in combination with the large increase in machine luminosity, promises an exploration of $\tau$ and charmed particles with unparalleled sensitivity.

# References


[1] A.Seiden, *Physics Summary*, these Proceedings.

[2] J.Kirkby, *Backgrounds to $\tau$ studies below charm threshold*, these Proceedings.

[3] K.L.Brown, T.Fieguth and J.M.Jowett, *Machine Physics Summary*, these Proceedings.

[4] J.Thaler, *Triggers at a $\tau$-charm Factory*, these Proceedings.

[5] K.Sliwa, *$\tau$-charm Factory Data Acquisition and Offline Requirements*, these Proceedings.

[6] P.Kim, private communication, and R. Schindler, these Proceedings.

[7] K.K.Gan, these Proceedings.

[8] A.J.Weinstein, *Central Tracking Design for a $\tau$-charm Factory*, these Proceedings.

[9] A.Seiden and J.Va'vra, private communication.

[10] M.S.Alam, private communication.

[11] S.C.Berridge et al., IEEE Trans. Nucl. Sci. 36 (1989) 339.

[12] G.Gladding, these Proceedings.

[13] J.Va'vra, *Particle Identification using $dE/dx$ Technique*, these Proceedings.

[14] R.Stroynowski, *Time of Flight Technique*, these Proceedings.

[15] B.N.Ratcliff, *Design Considerations for a Cerenkov Ring Imaging Detector at the $\tau$-charm Factory*, these Proceedings.